ACS APPLIED MATERIALS & INTERFACES

www.acsami.org

Research Article

Fabrication of NiCo Bimetallic MOF Films on 3D Foam with Assistance of Atomic Layer Deposition for Non-Invasive Lactic Acid Sensing

Zihan Lu,[#] Xinyi Ke,[#] Zhe Zhao,[*] Jiayuan Huang, Chang Liu, Jinlong Wang, Ruoyan Xu, Yongfeng Mei, and Gaoshan Huang[*]

Cite This: *ACS Appl. Mater. Interfaces* 2024, 16, 14218−14228

Read Online

ACCESS | Metrics & More | Article Recommendations | Supporting Information

ABSTRACT: Lactic acid (LA) is an important downstream product of glycolysis in living cells and is abundant in our body fluids, which are strongly associated with diseases. The development of enzyme-free LA sensors with high sensitivity and low consumption remains a challenge. 2D metal−organic frameworks (MOFs) are considered to be promising electrochemical sensing materials and have attracted much attention in recent years. Compared to monometallic MOFs, the construction of bimetallic MOFs (BMOFs) can obtain a larger specific surface area, thereby increasing the exposed active site. 3D petal-like Ni_xCo_y MOF films on nickel foams (Ni_xCo_y BMOF@Ni foams) are successfully prepared by combining atomic layer deposition-assisted technology and hydrothermal strategy. The established Ni_xCo_y BMOF@Ni foams demonstrate noticeable LA sensing activity, and the study is carried out on behalf of the Ni_1Co_5 BMOF@Ni foam, which has a sensitivity of up to 9030 μA mM^{-1} cm^{-2} with a linear range of 0.01−2.2 mM and the detection limit is as low as 0.16 μM. Additionally, the composite has excellent stability and repeatability for the detection of LA under a natural air environment with high accuracy and reliability. Density functional theory calculation is applied to study the reaction process between composites and LA, and the result suggests that the active site in the NiCo BMOF film favors the adsorption of LA relative to the active site of monometallic MOF film, resulting in improved performance. The developed composite has a great potential for the application of noninvasive LA biosensors.

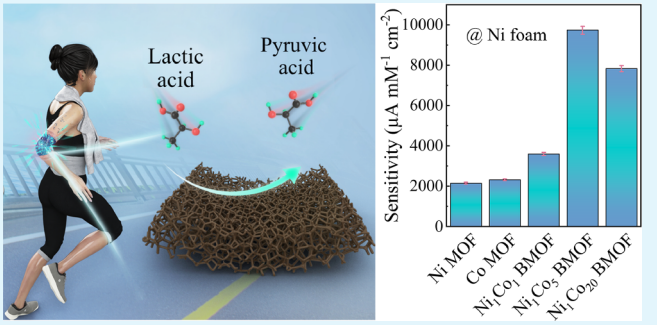

KEYWORDS: *bimetallic MOF film, biosensor, electrochemical sensing, lactic acid, nickel foam, active site, atomic layer deposition*

INTRODUCTION

With the development of personal diagnostic technology, the potential of real-time, continuous, and noninvasive monitoring has received widespread attention. In recent years, various health-related sensors have been extensively investigated.[1−3] Lactic acid (LA) monitoring is becoming greatly important in clinical diagnosis, as it is regarded as the second lowest molecular weight metabolite after glucose.[4,5] LA is a byproduct of glycolysis and anaerobic glucose metabolism that is considered as a marker of hypoxia as well as a potential indicator of stress ischemia, panic disorder, and cystic fibrosis.[5] Currently, most clinical medical diagnoses rely on blood analysis using huge, complex, and time-consuming instruments in large laboratories.[6] LA blood tests are conducted by invasive methods on collected samples, followed by chemical analysis of centrifugated plasma. In addition, traditional medical models require patients to go to the hospital, which could adversely cause delayed diagnosis and treatment, especially in emergency situations.[7] In fact, most healthcare monitoring is carried out through invasive diagnostic tools, which hinders precise real-time tracking of an individual's physiological health.[8] In order to continuously monitor a patient's health for prognosis and treatment, it is critical to rely on noninvasive health-tracking devices. Therefore, various LA detection methods have been reported, such as spectrophotometric detection, chemical oxidizing lactate methods, and electrochemical sensors.[9−11] To this end, both enzymatic and nonenzymatic approaches have been developed. Although the enzymatic method supports incomparable detection performance in terms of selectivity and sensitivity, its applications are limited due to its high cost and susceptibility to environmental factors.[12] The development of sensing technologies by using enzyme-free sensing materials can overcome the inherent shortcomings of

Received: January 27, 2024
Revised: February 24, 2024
Accepted: February 26, 2024
Published: March 11, 2024

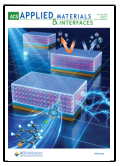

https://doi.org/10.1021/acsami.4c01573
ACS Appl. Mater. Interfaces 2024, 16, 14218−14228

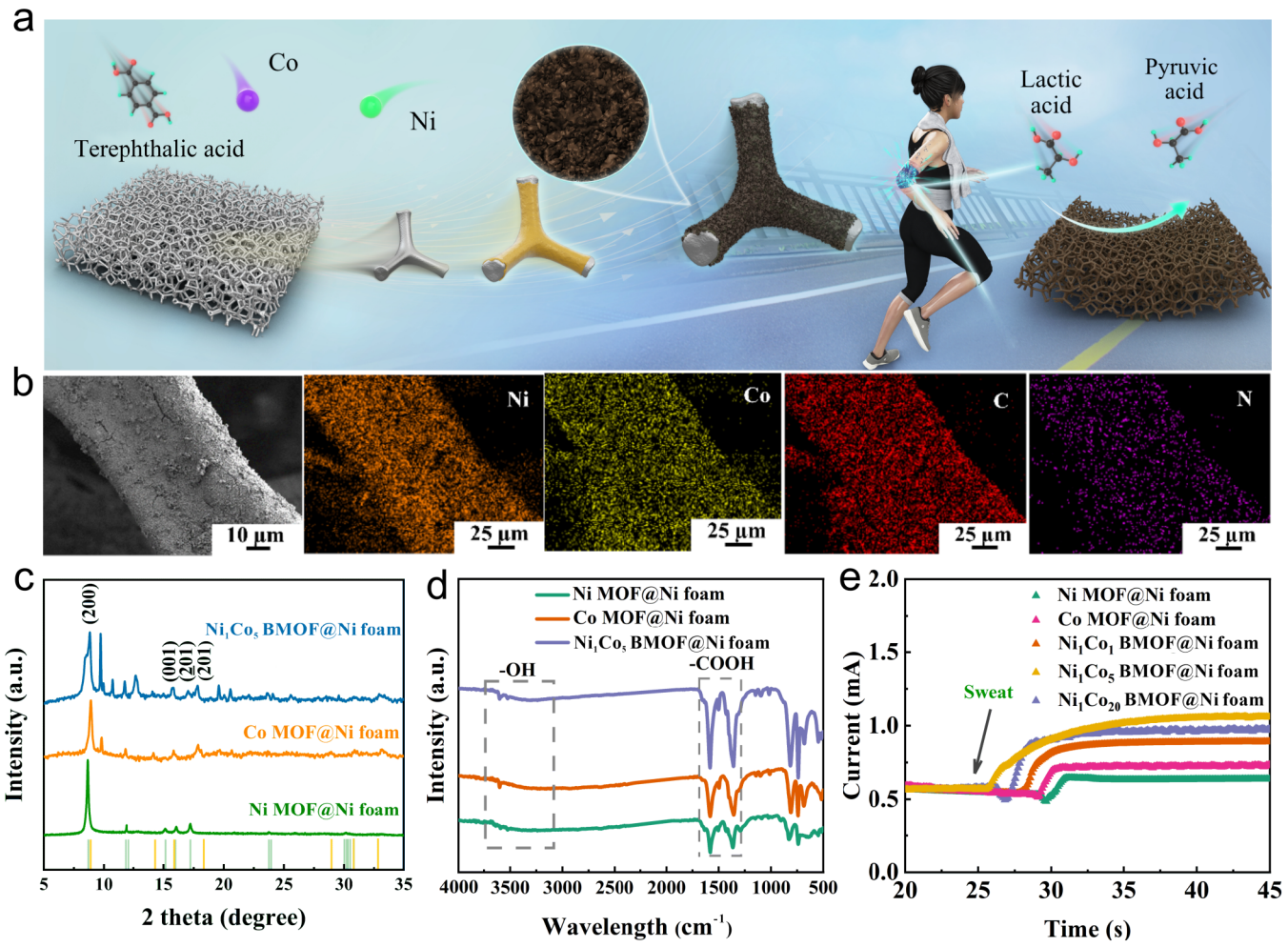

Figure 1. (a) Illustration of the whole work. (b) EDS mapping of the Ni_1Co_5 BMOF@Ni foam. (c) XRD patterns of the Ni MOF@Ni foam, Co MOF@Ni foam, and Ni_1Co_5 bMOF@Ni foam. (d) FTIR curves of the Ni MOF@Ni foam, Co MOF@Nifoam, and Ni_1Co_5 BMOF@Ni foam. (e) *I*−*t* curves of samples with the addition of artificial sweat.

enzyme-free sensing and provide accurate judgment, which is a win−win research pathway and therefore has broader prospects.[13] In addition, LA lacks special chemical activities, such as redox reaction, optical effects, and electrochemical activity, which poses a challenge to the development of nonenzymatic lactate sensors.[11] Few examples currently reported indicate that due to complex instruments and time-consuming steps, convenient health monitoring is less promising. A novel nonenzymatic approach for simple and efficient discrimination of LA remains in short supply and in great demand.

Based on previous reports, metal−organic frameworks (MOFs) have well demonstrated their potential for molecular sensing.[13,14] The open-access pore structure and highly customizable capabilities of MOFs make them an ideal choice for developing advanced sensors.[15] Combining the advantages of inorganic and organic materials, MOFs have received a lot of attention as versatile electronic and photoelectric catalytic platforms. This is determined by the complex characteristics of MOFs, including extraordinary surface area, exceptional porosity, customizable pore size, enormous structural, chemical tunability, and presynthesis and postsynthesis structural modification.[16−20] Bimetallic MOFs (BMOFs) and their composites offer more advantages than monometallic compounds, including increased conductivity, extended active sites, high charge capacity, and adjustable electrochemical activity.[21,22] BMOFs can also be combined with other electrochemically active materials to produce advanced composites with larger specific area, higher conductivity, and superior dispersion.[23,24] This provides a potential material option for the aforementioned LA detection with less chemical activities. Additionally, although BMOFs could constitute a nanoscale 3D confined space, the assembly configuration on the sensing electrodes is still a 1D or 2D structure, which limits their sensing applications for complex biological targets.[25,26] Similarly, the structure of these electrodes limits the stability of the active components, making them susceptible to leakage due to their small surface area and poor adhesion. Moreover, the planar electrode structure cannot provide sufficient surface area for ion diffusion and interaction, reducing signal transmission capacity.[27−29] In order to improve the performance of the electrode, fabrication of 3D structure/BMOFs composite is explored.[30] Although advantageous devices have been preliminary demonstrated, there are still many problems that need to be addressed, such as weak adhesion and ununiform growth.[31,32] As illustrated in our previous works, there was an efficient strategy developed for integrating MOF films into complex conductive substrates via induction of oxide nanomembrane prepared by atomic layer deposition (ALD).[33] ALD technology enables the deposition of uniform and

https://doi.org/10.1021/acsami.4c01573
ACS Appl. Mater. Interfaces 2024, 16, 14218−14228

conformal metal oxide nanomembranes with controlled thickness on a variety of substrates, including silicon wafers, carbon materials, and polymers.,[34−36] Thanks to gaseous deposition, metal oxide nanomembranes can be uniformly grown on the complex 3D structures.[37] By using the following hydrothermal reaction, the oxide nanomembrane could be transformed into the target MOF film, which can uniformly and firmly attach to the substrates. The advantages of ALD-assisted growth of MOF film approach are mainly manifested in the following aspects.[38] First, the adhesion between the film and the substrate is enhanced, providing the composite an excellent structural stability. Second, uniform assembly avoids the aggregation of particles. Third, ALD technology shows high controllability and universal applicability, which could be applied to different MOFs and substrates. Therefore, these advantages give composites an enhanced electrochemical performance. It is worth noting that the strategy is mostly used for the preparation of monometallic MOFs-based sensing, and its application in the field of BMOFs-based biosensing still needs to be explored.

Here, BMOF film-based enzyme-free sweat LA sensors were prepared by ALD-assisted induction. The structure was prepared by growing a BMOF film on ALD-pretreated Ni foam and is named as the NiCo BMOF@Ni foam. NiCo BMOF films with different metal mass proportions were produced on the surface of the 3D frame of the Ni foam to form a nanopetal-like structure. In the resulting 3D foam composite, the conductive Ni foam substrate significantly enhances charge transport. The assembly of the functional films maintains the original coordination and nanoporous structure of NiCo BMOFs. Compared to monometallic MOF films, NiCo BMOF films provide a larger specific surface area and more abundant active sites. Therefore, our NiCo BMOF@Ni foam exhibits excellent LA detecting performance with an ultrahigh sensitivity of 9030 mA $mM^{-1}cm^{-2}$ in a relatively low LA concentration (0.01−2.2 mM) and a low limit detection (LOD) of 0.16 μM. The rapid current response of prepared device to various LA concentrations confirmed its real-time applications. Additionally, theoretical calculations were performed to further explain the experimental phenomenon and sensing mechanism. The results could help us to further understand the biosensing mechanism, and we believe that this work opens up new possibilities for the development of portable highly sensitive enzyme-free LA sensors; thus, it has great prospects for development in the future.

RESULTS AND DISCUSSION

Assembly and Characterization of the Ni_xCo_y BMOF@Ni foam. In this work, NiCo BMOF@Ni foam samples were named according to the different metal components, such as Ni MOF@Ni foam, Ni_1Co_1 BMOF@Ni foam, Ni_1Co_5 BMOF@Ni foam, Ni_1Co_{20} BMOF@Ni foam, and Co MOF@Ni foam. Here, the Ni:Co ratio was varied to determine the optimal value for the best electrochemical sensing performance, as will be discussed later. Figure 1a shows a demonstration of this work. According to our recent experiments, ZnO nanomembranes exhibit the best effect for assisting the assembly of the MOF film.[34] Thus, ZnO nanomembranes (yellow layer in Figure 1a) supported on foam is first prepared via ALD technology to assist the growth of subsequent NiCo BMOF films with solid adhesion. The produced NiCo BMOF@Ni foam is then applied to detect human sweat and the concentration of LA in sweat is expressed via electrochemical signals. The morphologies of these composite foams are investigated by scanning electron microscopy (SEM). The results indicate that NiCo BMOF films are uniformly loaded onto the substrate surface through a hydrothermal method (Figure 1b). Through variation of the weight ratios of Ni and Co, a series of composite foams with different Ni and Co loading amounts (i.e., the Ni_xCo_y BMOF@Ni foam) are prepared (Figures S1−S5). From the enlarged SEM images, it can be seen that they all exhibit petal-like multilayered structures on the substrate. As the amount of Co increases, the size of nanosheets decreases and more nanosheets are assembled on the foam. Additionally, the energy-dispersive spectroscopy (EDS) patterns of the Ni_1Co_5 BMOF@Ni foam in Figure 1b further display uniform distribution of the elements Ni, Co, C, and N throughout the whole surface of substrate. In this fabrication approach, the adhesion between the ZnO nanomembrane and the substrate imparts excellent structural stability, thus optimizing the entire fabrication process. SEM image in Figure S6 illustrates the interface between the Ni_1Co_5 BMOF film and Ni foam. It is evident that the Ni_1Co_5 BMOF film tightly grows on the substrate, confirming the outstanding connection between BMOF film and substrate. For comparison, we also tried to prepare NiCo BMOF on the Ni foam without the ZnO nanomembrane. Figure S7 reveals that the NiCo BMOF film did not grow on the Ni foam, demonstrating the significant influence of the ALD ZnO nanomembrane on the fabrication of the NiCo BMOF@Ni foam. Specifically, according to our previous investigation,[19] the ALD ZnO nanomembrane that is closely connected with the substrate surface is involved in the hydrothermal growth of BMOF particles, leading to a very good adhesion between BMOF film and substrate.

The structures of the samples are further studied by X-ray diffraction (XRD). The XRD patterns of the Ni MOF@Ni foam, Co MOF@Ni foam, and Ni_1Co_5 BMOF@Ni foam are recorded and shown in Figure 1c. The standard XRD patterns of Ni and Co MOFs (Figures S8 and S9) are also plotted in light green and light yellow for comparison. For the Ni_1Co_5 BMOF@Ni foam, besides the diffraction peaks from the Ni foam (Figure S10), four prominent peaks can be observed, which are associated with (200), (001), (201), and ($\bar{2}$01) lattice planes of NiCo BMOFs, suggesting the presence of Ni MOFs and Co MOFs. The Fourier transform infrared (FTIR) results are displayed in Figure 1d. As for monometallic MOFs and BMOFs, the spectra are virtually identical:[39] the bands around 3605 and 3525 cm^{-1} belong to the −OH functional group stretching vibration, the peaks at 1595 and 1379 cm^{-1} correspond to the COOH functional group asymmetric and symmetric stretching vibration, respectively, and the peaks at 820 and 740 cm^{-1} correspond to the vibration of the C−H group. Especially, the band around 540 cm^{-1} is consistent with the dicarboxylate group's bridge characterization of metal ions, indicating the presence of metal centers in organic frameworks.[39] Moreover, it also indicates that the introduction of Ni foams during the chemical process does not influence the coordination between metal ions and organic bridges, and these results agree with the aforementioned XRD results. Here, we notice that different metal ions incorporated lead to a significant tunability of the electrochemical property. Figure 1e illustrates the $I-t$ curves of samples with the addition of 10 μL of artificial sweat in 0.1 M NaOH solution at a potential of 0.5 V. With the addition of sweat, rapid current responses are displayed due to the change in the valence state of the metal.

https://doi.org/10.1021/acsami.4c01573
ACS Appl. Mater. Interfaces 2024, 16, 14218−14228

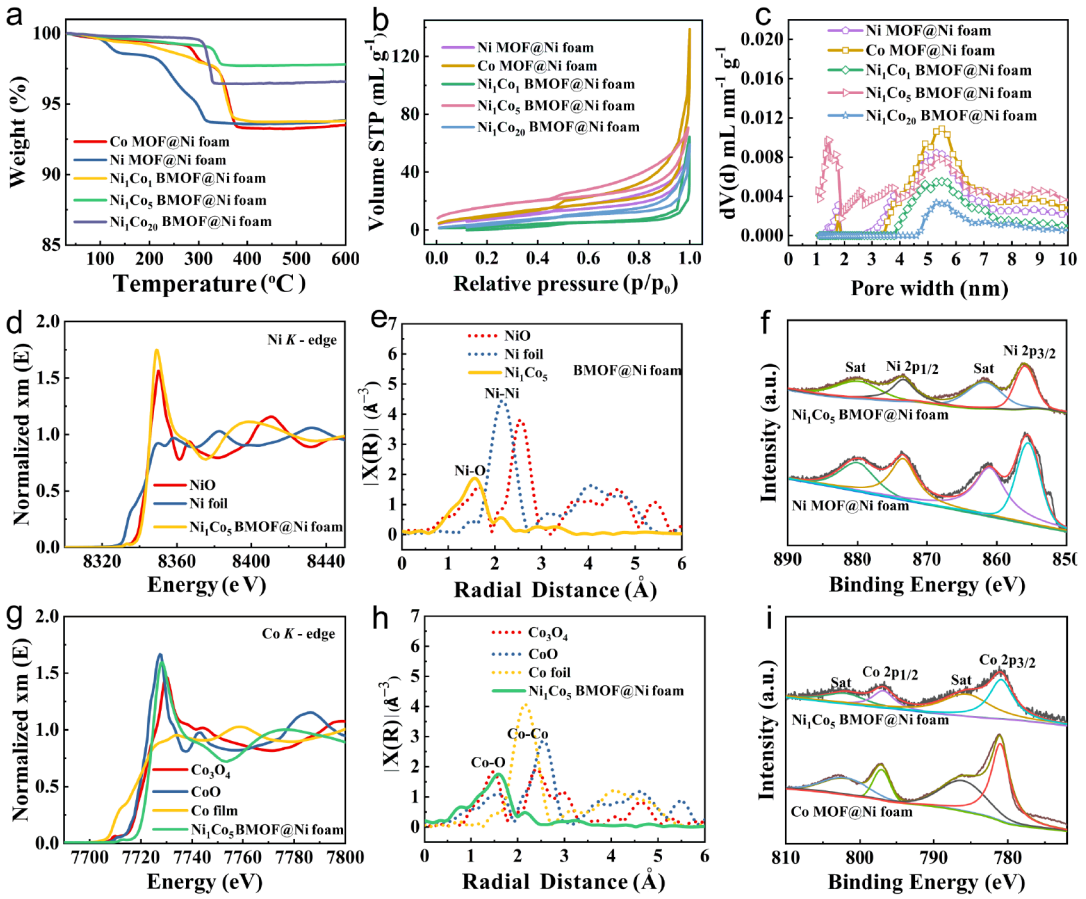

Figure 2. (A) TGA curves of prepared composites. (b) N_2 adsorption−desorption isotherms of the samples. (c) Pore size distribution of corresponding samples. (d) Normalized XANES curve of the Ni_1Co_5 BMOF@Ni foam at the Ni K-edge with NiO and Ni foil as references. (e) Corresponding k^3-weighted EXAFS spectra. (f) High-resolution Ni 2p spectra of the Ni MOF@Ni foam and Ni_1Co_5 BMOF@Ni foam. (g) Normalized XANES curve of the Ni_1Co_5 BMOF@Ni foam at the Co K-edge with Co_3O_4, CoO, and Co foil as references. (h) The corresponding k^3-weighted EXAFS spectra. (i) High-resolution Co 2p spectra of the Ni MOF@Ni foam and Ni_1Co_5 BMOF@Ni foam.

As the content of Co increases, the current response becomes more rapid, and is the most ideal when the content of Co is 5 times that of Ni. However, when the amount of Co is further increased, the response to LA decreases. The detailed characterization and mechanical investigation will be presented later.

Structure Analysis. Furthermore, the thermal stability of prepared NiCo BMOF@Ni foams is investigated by using thermogravimetric analysis (TGA) (Figure 2a). It can be seen that when the temperature is greater than ~300 °C, there is a great decrease in weight, which is possibly ascribed to the oxidation degradation of organic linkers. It has also been proved that composite foams have excellent structural stability for applications across a wide temperature range. Moreover, the results indicate that higher Co content can maintain better thermostability, which is beneficial for the following electrochemical detection. Additionally, the Brunauer−Emmett−Teller (BET) surface area and corresponding pore distributions are obtained, as shown in Figure 2b,c and Table 1. It can be observed that all composite foams show type I and type IV isotherms,[40] indicating that micropores and mesopores coexist in all NiCo BMOF@Ni foams. The pore size distributions demonstrate a microporous structure within 1.3 to 1.8 nm, and apparent mesopore peaks at about 2.5, 3.5, and 5 nm are also noticeable. According to our previous investigations, the micropores are mainly ascribed to the pores of MOFs, and

Table 1. Surface Area and Pore Size Distribution of the NiCo BMOF@Ni foam Samples

sample	specific surface area ($m^2\ g^{-1}$)	micropore volume (mL g^{-1})	mesopore volume (mL g^{-1})	total pore volume (mL g^{-1})
Ni MOF@Ni foam	32	0.0007	0.0593	0.06
Co MOF@Ni foam	38	0.0015	0.0985	0.10
Ni_1Co_1 BMOF@Ni foam	25	0	0.05	0.05
Ni_1Co_5 BMOF@Ni foam	58	0.007	0.083	0.09
Ni_1Co_{20} BMOF@Ni foam	18	0	0.02	0.02

the stackable MOF particles on the surface of foams produce mesopores.[32] Additionally, the adsorption and desorption isotherms also show that the Ni_1Co_5 BMOF@Ni foam represents a large specific surface area of 58 m^2g^{-1} with a great total pore volume of 0.09 mL g^{-1}. After continually increasing the Co content, the composite foam presents a reduced surface area of 18 m^2g^{-1} with a total pore volume of 0.02 mL g^{-1}. This might be due to the larger diameter of the

https://doi.org/10.1021/acsami.4c01573
ACS Appl. Mater. Interfaces 2024, 16, 14218−14228

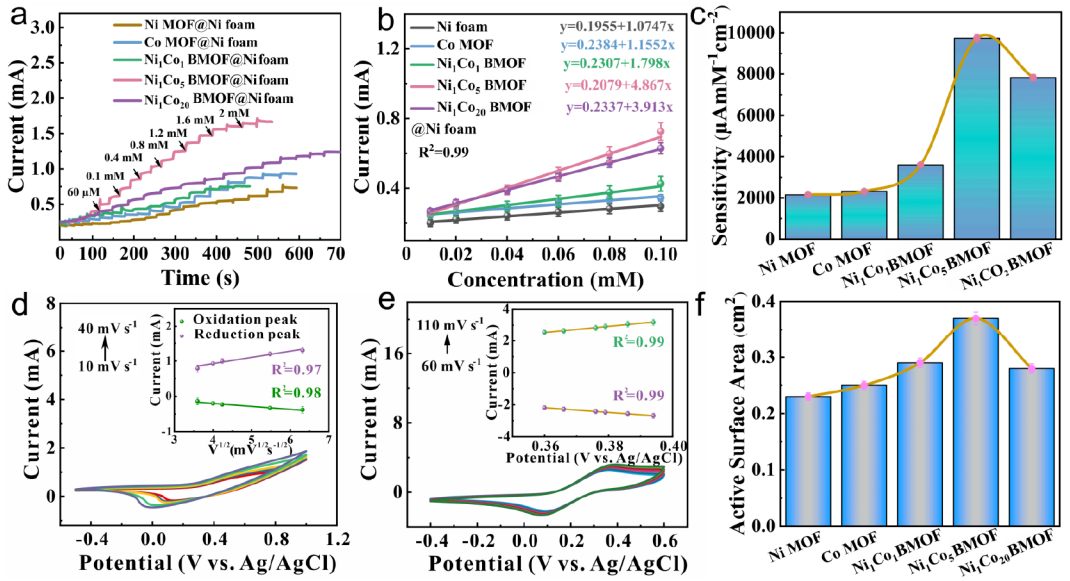

Figure 3. (a) Chronoamperometry measurements of the Ni MOF@Ni foam, Co MOF@Ni foam, Ni_1Co_1 BMOF@Ni foam, Ni_1Co_5 BMOF@Ni foam, and Ni_1Co_{20} BMOF@Ni foam with successive addition of LA with different concentrations in 0.1 M NaOH solution at 0.5 V. (b) Calibration plots derived from (a). (c) The corresponding sensitivities derived from (b). (d) CV scans with various scan rates from 10 to 40 mV s^{-1} in a 0.1 M NaOH solution containing 1 mM LA of Ni_1Co_5 BMOF@Ni foam (the inset is the corresponding calibration plot). (e) CV scans with various scan rates from 60 to 110 mV s^{-1} in 0.1 M NaOH solution containing 5 mM $K_3[Fe(CN)_6]$ of Ni_1Co_5 BMOF@Ni foam (the inset is the corresponding calibration plot). (f) The corresponding calculated active surface area of the samples.

BMOF particles, which leads to a decrease in the overall specific surface area.

The coordination environment of the produced composites is investigated via element selective X-ray absorption spectroscopy (XAS). X-ray absorption near-edge structure (XANES) and extended X-ray absorption fine structure (EXAFS) analyses provide a better understanding of valence and coordination states of metal atomic centers. As illustrated in the XANES curves of the Ni_1Co_5 BMOF@Ni foam, the absorption energy of Ni *K*-edge is almost similar to that of the NiO reference. It is considered that the main valence state of Ni in the composite is around +2 (Figures 2d and S11). Similarly, the Co *K*-edge XANES spectra show that the near-edge absorption energy of the prepared composite is placed between Co_3O_4 and CoO references. However, this absorption energy is closer to that of the latter, indicating that the main valence state of Co of the produced composite foam is slightly greater than +2 (Figures 2g and S12). The positive charge centers of Ni and Co could be attributed to the adjacent N partially depleting their free electron atoms through valence bonds.[27] The coordination environments are further investigated by k^3-weighted Fourier transform (FT) EXAFS spectra of the composite (Tables S1 and S2). Figure 2e displays peaks at 1.56 and 2.14 Å, which correspond to scattering paths with Ni−O and Ni−Ni, respectively. Moreover, as shown in Figure 2h, peaks at 1.59 and 2.14 Å correspond to the scattering paths with Co−O and Co−Co, respectively. These results suggest that the atomic dispersion of Ni and Co is isolated.[27] Additionally, the wavelet transform (WT) contour plots of Ni and Co in the composite samples disclose an intensity maximum of ∼4 $Å^{-1}$, corresponding to Ni−O and Co−O coordination in the composite (Figures S13 and S14). Furthermore, the chemical composition of composite foams is investigated by X-ray photoelectron spectroscopy (XPS), which discloses the presence of Ni, Co, O, and C (Figure S15). The high-resolution Ni 2p XPS spectrum presents metallic Ni characteristic peaks at 873.28 eV (Ni $2p_{1/2}$) and 855.93 eV (Ni $2p_{3/2}$) (Figure 2f). Similarly, the high-resolution Co 2p XPS spectrum presents metallic Co characteristic peaks at 796.83 eV (Co $2p_{1/2}$) and 781.08 eV (Co $2p_{3/2}$) (Figure 2i). These results confirm the coexistence of Ni and Co in the composite. Also, Figure S16 shows the high-resolution O 1s spectra of Co MOF@Ni foam, Ni MOF@Ni foam, and Ni_1Co_5 BMOF@Ni foam. The most intense shoulder peak in the Ni_1Co_5 BMOF@Ni foam, which appears at a lower binding energy side, indicates the highest concentration of oxygen vacancy in the Ni_1Co_5 BMOF film compared to monometallic MOF films.[41]

Electrochemical Evaluation. Considering the potential application of these bimetallic centers with atomic structure in electrocatalysis, the nonenzymatic LA detection performance of the composites is evaluated. First, we study the sensing performance of the composites by *I*−*t* curves. Figure S17 displays the effect of the imposed potential on the current response. It is obvious that all our produced composites exhibit a remarkable and stable current response at 0.5 V. Therefore, the detailed *I*−*t* measurements of the NiCo BMOF@Ni foam electrode are performed at 0.5 V. Figure 3a illustrates the *I*−*t* recording of the composite sensors with the consecutive addition of LA in a 0.1 M NaOH solution. It is worth noting that the contributions from the Ni foam can be neglected, as shown in Figure S18, and the ZnO nanomembrane on the Ni foam (i.e., ZnO@Ni foam) is also found to be electrochemically inactive (Figure S19). The current experiments demonstrate apparent and rapid current responses of the composites containing NiCo BMOF films, implying a real-time LA detecting ability of NiCo BMOF films. Specifically, the typical response time is determined to be ∼0.18 s (Figure S20), clearly illustrating its exceptional rapid response. The corresponding calibration curves for LA detection are shown in Figure 3b. According to the calibration graph, these composites have high sensitivity, with a linear relationship at low concentrations of 0.01−0.1 mM (the linear regression

https://doi.org/10.1021/acsami.4c01573
ACS Appl. Mater. Interfaces 2024, 16, 14218−14228

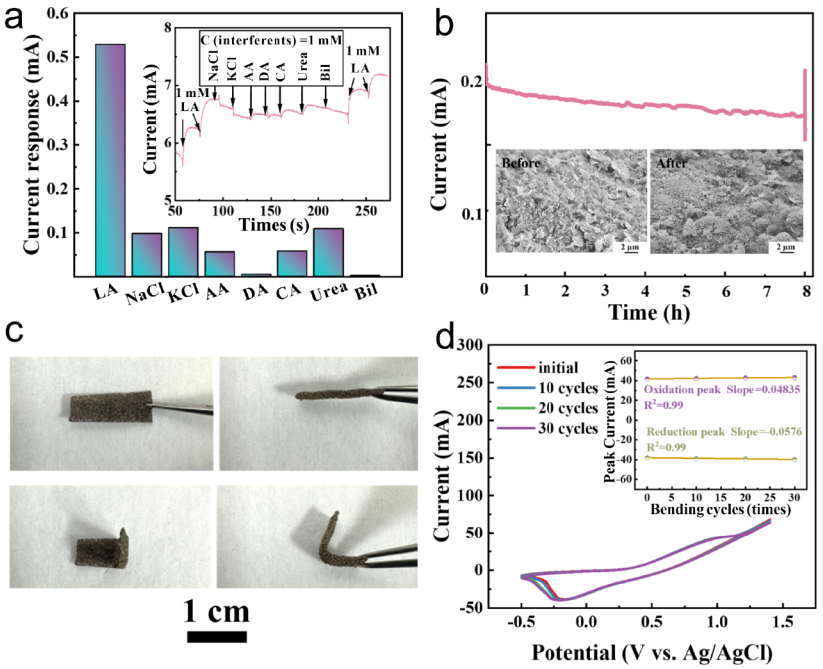

Figure 4. (a) Current responses of the Ni_1Co_5 BMOF@Ni foam toward 1 mM LA, 1 mM NaCl, KCl, 1 mM AA, 1 mM DA, 1 mM CA, 1 mM urea, and 1 mM Bil at 0.5 V. The inset shows the chronoamperometry measurements of the Ni_1Co_5 BMOF@Ni foam with the successive addition of LA and other interferents. (b) I–t curve of the Ni_1Co_5 BMOF@Ni foam in 0.1 M NaOH solution with 1.0 mM LA at 0.5 V. 1 mM LA was dropped into the solution after 8 h to measure the recovery performance (the inset shows the morphology of the sample before and after the 8 h test). (c) The photographs of the composite foam before and after 90° bending. (d) CV curves of the composite over up to 30 bending cycles in 0.1 M NaOH solution containing 1 mM LA (the inset is the corresponding calibration plots of the peaks).

equation and relative correlation coefficient (R^2) are shown in Figure 3b). The sensitivity could reach about 9030 μA $mM^{-1}cm^{-2}$ (for the Ni_1Co_5 BMOF@Ni foam, Figure 3c). Additionally, according to the equation: limit of detection (LOD) = $3\delta/S$, where δ is a standard deviation and S is the sensor sensitivity, LOD could be as low as 0.16 μM for the Ni_1Co_5 BMOF@Ni foam-based sensor. It is worth noting that the prepared composite-based sensor not only shows high sensitivity in low concentrations of LA, but also maintains good sensitivity in a high concentration environment (Figure S21). In addition, the performance of current sensor is higher than those of electrochemical LA sensors reported in previous publications. For instance, as summarized in Table S3, the sensitivity of the Ni_1Co_5 BMOF@Ni foam sensor is at least several times higher. The reason for the excellent performance might be due to the fact that the Ni_1Co_5 BMOF film on the surface of foam possesses more active sites associated with large surface area and abundant oxygen vacancies.[41] In addition, the different weight ratios of Ni and Co in the bimetallic center also change the geometry and electronic structure of the active species, and thus the catalytic activity.[42] The experimental results in Figure 3c also indicate that there is an optimal value of ratio of Ni and Co for enhanced electrochemical property,[27] which is of 1:5 (Ni:Co) in current work. Further increase in the Co or Ni content will lead to a decrease in the LA sensing performance.

Subsequently, the electrochemical performance of the Ni_1Co_5 BMOF@Ni foam is further investigated via cyclic voltammetry (CV) in 0.1 M NaOH solution with 10 mV s^{-1} scanning rate in −0.8 to 1.4 V potential range. As displayed in Figure S22, the oxidation peak at ∼0.5 and the reduction peak at ∼0.1 V are related to the oxidation and reduction processes of the composite, respectively. It should be noted that in the electrolyte containing 1 mM LA, the current responses of the reduction peak and the oxidation peak are significantly enhanced, suggesting that the composite can generate additional currents by catalyzing the oxidation of LA. According to the previous reports,[32] the additional current response could be attributed to the following reactions:

$$NiCo_2O_4 + OH^- + H_2O \rightarrow NiO(OH) + 2Co(OH) + e^- \quad (1)$$

$$CoO(OH) + OH^- \rightarrow CoO_2 + H_2O + e^- \quad (2)$$

$$Ni(III) + Co(IV) + \text{lactic acid} \rightarrow Ni(II) + Co(II) + \text{pyruvic acid} \quad (3)$$

Here, the reaction kinetics of the Ni_1Co_5 BMOF@Ni foam is investigated using CV scans with different scan rates (Figure 3d). It is obvious that with the increasing scan rate, the oxidation and reduction peak response currents increase continuously, which provides a good interpretation of the controlled response of LA.[20] Meanwhile, the inset of Figure 3d illustrates that in the 1 mM LA electrolytic solution, the enhanced response currents of the anodic oxidation peak and the cathodic reduction peak have a linear relationship with the square root of the scan rate from 10 to 40 mV s^{-1}. These confirm the presence of diffusion-controlled electrochemical process of the composite.[20]

In order to further estimate the electrochemical performance of the NiCo BMOF@Ni foam quantitatively, the active surface area of the prepared composite foams is analyzed through a $K_3[Fe(CN)_6]$ probe. Figure 3e shows the values of the Ni_1Co_5 BMOF@Ni foam, and a group of oxidation and reduction peaks could be observed under different CV scanning rates and

https://doi.org/10.1021/acsami.4c01573
ACS Appl. Mater. Interfaces 2024, 16, 14218−14228

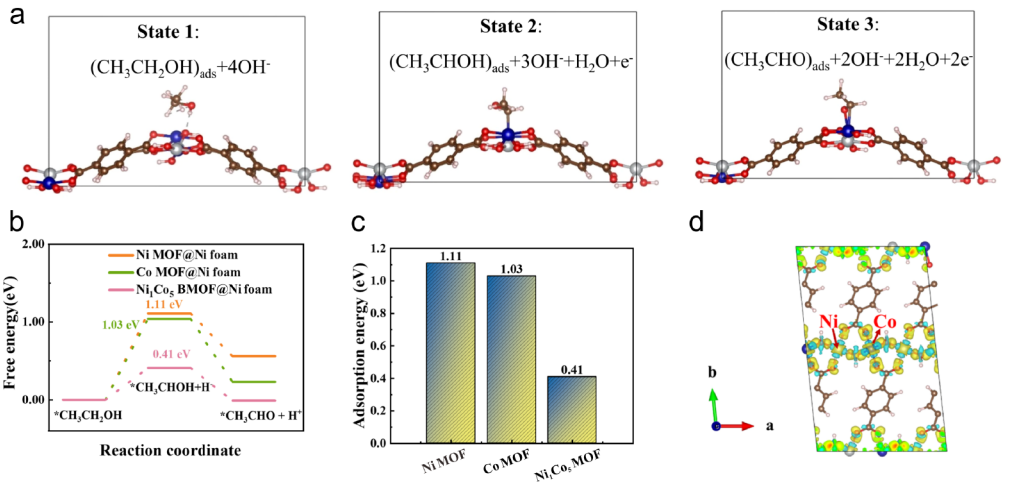

Figure 5. (A) DFT calculated models of NiCo BMOFs adsorbed with the reactive species from different LA sensing reaction states. (b) DFT calculated free energy profiles of the LA sensing reaction over monometallic MOFs and NiCo BMOFs. (c) The corresponding free energy of state 2. (d) The charge density difference of monometallic MOFs and NiCo BMOFs and the yellow and blue color parts indicate charge accumulation and depletion, respectively.

the response currents of these peaks is enhanced on increasing the scan rate from 60 to 110 mV s^{-1}. The characterizations of other composites are summarized in Figure S23 and the increasing trend is similar to that of the Ni_1Co_5 BMOF@Ni foam. In this work, the active area (S) of detection electrode is calculated according to the Randles−Sevcik formula:[33]

$$I_{peak} = (2.69 \times 10^5)n^{3/2}SD^{1/2}\ Cv^{1/2} \quad (4)$$

where n is the amount of transferred electrons, D and C are the diffusion coefficient and bulk concentration of $K_3[Fe(CN)_6]$, respectively. Therefore, a series of S are evaluated to be 0.23, 0.25, 0.29, 0.37, and 0.28 cm^2 for the produced composite electrodes according to the slope of peaks response current and the square root of scanning rate (Figure 3f). It is obvious that the active area is enhanced with the increasing Co content, which may be attributed to a larger specific surface area and more abundant active sites of the BMOF film. This is beneficial to the interaction of active matter in the electrolyte and the transfer of interfacial electrons, improving the electrochemical performance. The excellent LA sensing performance of the prepared NiCo BMOF@Ni foam may be further ascribed to the following essential factors. First, as mentioned before, oxide nanomembranes induce assembly of the BMOF film leading to strong adhesion and uniform coating, and NiCo BMOF particles are tightly stacked to form a dense functional film. This could greatly enhance the structural stability. Second, the multiple conductive pathways in the 3D conductive substrate promote electron transfer, which further improves the sensing performance.

Anti-interference performance is also a significant factor for a practical LA sensor.

The $I-t$ curve of the Ni_1Co_5 BMOF@Ni foam with consecutive introduction of 1 mM LA, 1 mM NaCl, 1 mM KCl, 1 mM ascorbic acid (AA), 1 mM dopamine (DA), 1 mM urea, and 1 mM bilirubin (Bil) is shown in Figure 4a. It can be seen that the current response of the target LA is obvious. However, for the addition of interferents, only a negligible response could be observed. On the other hand, glucose is always an important biomass in sweat, and corresponding sensing experiments in Figure S24 evidence that when 5 mM glucose is added, there is a negligible current response. Thus, the presence of glucose in sweat will not adversely affect the performance of the sensor. In addition to biomass interference, the temperature is also a significant factor. We raised the temperature of testing solution (PBS) to 348 K and found that the effect of temperature on our sensor is scarcely noticeable (Figure S25). Moreover, the electrochemical stability is also analyzed in 1 mM LA solution at 0.5 V. As shown in Figure 4b, the composite exhibits a stable current response at about 0.17 mA for 8 h, and the inset of Figure 4b also displays the morphological stability of the composite after 8 h $I-t$ measurement. In addition, a stability test of even longer time is shown in Figure S26, and no peeling of the NiCo BMOF film can be observed, which further confirms that due to the assistance of ALD induction, the active layer can be firmly attached on the substrate. This result is also verified by the XPS result in Figure S15b. Moreover, we also perform the chronoamperometry measurement of the composite Ni foam for a period of 5 weeks; it indicates that although performance deteriorates over time, it still responds quickly to LA (Figure S27).

We hope our sensors can perform the function of daily monitoring, so we further tested their flexibility and evaluated their electrochemical performance after repeated 90° bending. As displayed in Figure 4c, the composite is bent to 90° and then returned to its original form for electrochemical performance testing. Figure 4d records the sensing performance of the flexible sensor on LA after multiple bending cycles. It shows that although there are slight changes, the sensor we prepared could still maintain good sensing performance toward the target LA after severe deformation. The values of oxidation and reduction peaks further demonstrate the stability of the sensor (inset of Figure 4d). The good sensing performance is mainly attributed to the following two reasons. First, ALD technology realizes a tight connection between the NiCo BMOF film and the substrate, reducing the risk of film falling off during deformation. Second, the porous structure provides a certain space for deformation, so that the BMOF film could accommodate some deformation.

Theoretical Calculation. The improved electrochemical activity of the NiCo BMOF@Ni foam is further clarified by density functional theory (DFT). Here, Ni MOFs were taken

https://doi.org/10.1021/acsami.4c01573
ACS Appl. Mater. Interfaces 2024, 16, 14218−14228

as the basis, and the (001) surface plane was used for catalysis. The repetitive unit of Ni MOFs was all included, which ensures the integrity of the electronic structure affecting the catalytic property. As for the structure of Co MOFs, all of the Ni atoms in Ni MOFs were replaced by Co atoms, wheras half of the Ni atoms were replaced by Co atoms in the case of NiCo BMOFs. In NiCo BMOFs, both Ni and Co were coordinated with O atoms, as evidenced by the synchrotron radiation result. The corresponding adsorption configurations are shown in Figures 5a and S28−S30. It is suggested that for individual Ni MOFs and Co MOFs, the reaction process would be interrupted due to the exclusive hydrogen bond when CH_3CHOH is formed.[43] As for active sites on monometallic MOFs, LA adsorbs on Ni or Co atoms and are prior to eliminate its methylene C−H bond during the reaction process.[11] On the contrary, for NiCo bimetallic sites on NiCo nanoparticles, present Co atoms facilitate the adsorption of LA on them rather than on Ni atoms, and let the dehydrogenation of LA much easier to break O−H bond initially instead of methylene C−H bond, adjusting the reaction procedure to a variant pathway.[27] Free energy profiles of reaction pathways for monometallic and NiCo BMOFs are described in Figure 5b,c. It can be observed that the reaction procedure of initial dehydrogenation of LA (state 2) over NiCo dual sites is easier than that over sites on the monometallic MOFs (1.11 and 1.04 eV vs 0.41 eV). The formed CH_3CHOH could eliminate the possibility of parallel reactions to CH_3CHO in the second dehydrogenation step (state 3), which coexists for the second dehydrogenation step of CH_3CHOH on the surface of BMOFs. Bader charge analysis is shown in Figure 5d, and it is suggested that Co and Ni transfer charges to the surrounding O atoms and Co transfers more charges than Ni. Therefore, dual sites of BMOFs can enhance the interaction with LA and thus alter the sensing reaction process into an energetically favorable pathway, which contributes to the preeminent activity of NiCo BMOFs compared to monometallic Ni or Co MOFs.

CONCLUSIONS

In summary, we present a Ni foam-based enzyme-free noninvasive biosensor for highly selective and sensitive monitoring of LA. The NiCo BMOF film with petal-like morphology was synthesized by combining the ALD approach and the hydrothermal solvent strategy and the induction layer prepared by ALD led to firm attachment between the NiCo BMOF film and surface of the Ni foam. Due to the interconnected conductive path of the hierarchical structure and the highly conductive substrate, NiCo BMOF@Ni foams exhibit better catalytic activity toward LA and have excellent selectivity and sensing performance. In particular, by optimizing the mass ratio of the metal, it is found that when the mass of Co is 5 times that of Ni, the detection limit is as low as 0.16 μM, and the sensitivity can reach to 9030 $\mu A\ mM^{-1}\ cm^{-2}$. DFT calculations suggest that the active site of the NiCo BMOFs favors the adsorption of LA relative to the active site of monometallic MOFs, allowing the NiCo BMOF@Ni foam to proceed more smoothly with a lower free energy. Therefore, our work provides an understanding of the role of NiCo sites in LA sensing and opens up new opportunities for the development of noninvasive LA sensor devices.

EXPERIMENTAL METHODS

Chemicals. All chemical materials and reagents were received from commercial supplies and used as obtained. Nickel nitrate hexahydrate ($Ni(NO_3)_2{\cdot}6H_2O$, AR, 99%), cobaltous nitrate hexahydrate ($Co(NO_3)_2{\cdot}6H_2O$, AR, 99%), terephthalic acid (TPA, AR, 99%), sodium hydroxide (NaOH, AR, 97%), and *N,N*-dimethylformamide (DMF, AR, 95%) were purchased from Aladdin (Shanghai, China). Deionized (DI) water was received from Millipore, Direct-Q5. Ni foam was purchased from Alibaba Ltd.

Fabrication of the ZnO@Ni foam. Deposition of the ZnO nanomembrane on the exposed surface of the Ni foam was performed at 150 °C in an ALD reactor. Diethylzinc (DEZ) and DI water were used as the precursors. A typical ALD cycle included a DEZ pulse (50 ms), waiting time (10 s), a N_2 purge (30 s), a DI water pulse (30 ms), a waiting time (10 s), and a N_2 purge (30 s). The thickness of the ZnO nanomembrane was precisely controlled by the number of ALD cycles.

Fabrication of the Ni MOF@Ni foam. A 50 nm ZnO layer was loaded on the Ni foam surface via ALD technology at 150 °C (ZnO@Ni foam). Then, a precursor solution (A solution) was prepared by dissolving 2.7 mmol of $Ni(NO_3)_2{\cdot}6H_2O$ in 20 mL of DMF and ZnO@Ni foam was placed into solution A. The mixture was put in the oven at 150 °C for 24 h. Afterward, the mixture was cooled to room temperature. To this mixture, 1 mmol TPA dissolved in 20 mL DMF was added slowly. The mixture was returned back to the oven at 150 °C for 24 h. The resulting composite was isolated in DI water via sonication machine for three times and dried at 60 °C for 24 h.

Fabrication of the Co MOF@Ni foam. A 50 nm ZnO layer was loaded on the Ni foam surface via ALD technology at 150 °C (ZnO@Ni foam). Then, a precursor solution (solution A) was prepared by dissolving 2.7 mmol of $Co(NO_3)_2{\cdot}6H_2O$ in 20 mL of DMF and ZnO@Ni foam was placed into solution A. The mixture was put in the oven at 150 °C for 24 h. Afterward, the mixture was cooled to room temperature. To this mixture, 1 mmol TPA dissolved in 20 mL DMF was added slowly. The mixture was returned back to the oven at 150 °C for 24 h. The resulting composite was isolated in DI water via sonication machine for three times and dried at 60 °C for 24 h.

Fabrication of NiCo BMOF@Ni foams. A 50 nm ZnO layer was loaded on the Ni foam surface via ALD technology under 150 °C (ZnO@Ni foam). Then precursor solutions (solution A) were prepared by mixing different ratios of $Ni(NO_3)_2{\cdot}6H_2O$ and $Co(NO_3)_2{\cdot}6H_2O$ in 20 mL of DMF at room temperature. With the complete dissolution of the precursor solutions, ZnO@Ni foams were immersed in the mixtures. Then, the samples were placed into the oven at 150 °C. After 24 h, the mixtures were taken out from the oven and cooled to room temperature. Solution B was prepared by mixing 1 mmol TPA in DMF (20 mL), which was added into the mixtures slowly. Subsequently, the mixtures were returned back to the oven at 150 °C. Finally, the resulted composite Ni foams were washed by using DI water for three times and dried at 60 °C for 24 h.

Microstructural Characterizations. SEM images were recorded by using a Ziess Sigma 300 SEM. EDX mapping were acquired by a Ziess Ultra 55 SEM at 20 kV. XRD curves were recorded by a Thermo Fisher ARL EQUINOX 3000 machine. XPS analysis were obtained by using an ESCALAB QXi XPS. BET (77 K) was performed by Micromeritics ASAP2420 instrument, and all results were obtained after pretreatment at 120 °C dynamic vacuum for 12 h. FTIR was performed by a Thermo Nicolet IS5 machine at room temperature. TGA was measured via STA8000 instrument with 10 °C/min speed under air environment.

X-Ray Adsorption Spectroscopy. EXAFS and XANES of catalysts at Ni and Co K-edge were measured on the beamline station at Shanghai Synchrotron Radiation Facility using a fluorescence excitation mode, with NiO and Ni foil and Co_3O_4, CoO, and Co foil as references, respectively. The analysis of results was performed by Athena and Artemis software.[44−47] WT was also employed using the software package developed by Funke and Chukalina, and a Morlet wavelet with $\kappa = 10$ and $\sigma = 1$ was used.

https://doi.org/10.1021/acsami.4c01573
ACS Appl. Mater. Interfaces 2024, 16, 14218−14228

Electrochemical Measurements. All electrochemical experiments were performed at room temperature with a three-electrode system via an electrochemical workstation (Chenhua, CHI-760E). The carbon rod and Ag/AgCl electrode (1.0 M KCl, 25 °C) served as the counter electrode and reference electrode, respectively. The samples were cut into 0.5 cm × 1.0 cm pieces and then clipped to the platinum electrode clamp. Nafion was used to improve the connection between the sample and the clamp.

Calculation Details. All calculations were performed by DFT with the Vienna ab initio simulation package (VASP) with the Perdew−Burke−Ernzerhof (PBE) generalized gradient approximation (GGA).[45] The kinetic energy cutoff was set as 450 eV. The electronic energy and the maximum forces were less than 10^{-2} eV and 0.05 eV/Å, respectively. The adsorption free energy (ΔG) is calculated to analyze the binding strength between the clusters and substrate, and it can be defined as follows:

$$\Delta G = G_{tot} - G_{molecule} - G_{host} \quad (5)$$

where G_{tot} is the adsorbed system energy, $G_{molecule}$ is the individual clusters summation energy, and G_{host} is the substate energy.[46]

■ ASSOCIATED CONTENT

Supporting Information

The Supporting Information is available free of charge at https://pubs.acs.org/doi/10.1021/acsami.4c01573.

SEM images of the Ni MOF@Ni foam, Co MOF@Ni foam, and Ni_xCo_y BMOF@Ni foam; cross-sectional SEM image of the Ni_1Co_5 BMOF@Ni foam; SEM image of sample prepared without the assistance of ALD; simulated XRD patterns of Ni MOFs and Co MOFs; enlarged XRD patterns of the Ni_1Co_5 BMOF@Ni foam; detailed EXAFS results and analyses; additional XPS results; additional electrochemical characterizations and sensing performances; optimization models for DFT calculation; fitting parameters used to analyze EXAFS results; comparison of performances of LA sensors (PDF)

■ AUTHOR INFORMATION

Corresponding Authors

Zhe Zhao − *Department of Materials Science & State Key Laboratory of Molecular Engineering of Polymers, Fudan University, Shanghai 200438, PR China; College of Biological Science and Medical Engineering, Donghua University, Shanghai 201620, PR China*; Email: zhezhao@dhu.edu.cn

Gaoshan Huang − *Department of Materials Science & State Key Laboratory of Molecular Engineering of Polymers, Fudan University, Shanghai 200438, PR China; Yiwu Research Institute of Fudan University, Yiwu, Zhejiang 322000, PR China; International Institute for Intelligent Nanorobots and Nanosystems, Fudan University, Shanghai 200438, PR China*; orcid.org/0000-0002-0525-7177; Email: gshuang@fudan.edu.cn

Authors

Zihan Lu − *Department of Materials Science & State Key Laboratory of Molecular Engineering of Polymers, Fudan University, Shanghai 200438, PR China; Yiwu Research Institute of Fudan University, Yiwu, Zhejiang 322000, PR China; International Institute for Intelligent Nanorobots and Nanosystems, Fudan University, Shanghai 200438, PR China; Shanghai Center of Biomedicine Development, Zhangjiang Hi-Tech Park, Shanghai 201203, PR China*

Xinyi Ke − *Department of Materials Science & State Key Laboratory of Molecular Engineering of Polymers, Fudan University, Shanghai 200438, PR China; Yiwu Research Institute of Fudan University, Yiwu, Zhejiang 322000, PR China; International Institute for Intelligent Nanorobots and Nanosystems, Fudan University, Shanghai 200438, PR China*

Jiayuan Huang − *Department of Materials Science & State Key Laboratory of Molecular Engineering of Polymers, Fudan University, Shanghai 200438, PR China; Yiwu Research Institute of Fudan University, Yiwu, Zhejiang 322000, PR China; International Institute for Intelligent Nanorobots and Nanosystems, Fudan University, Shanghai 200438, PR China*

Chang Liu − *Department of Materials Science & State Key Laboratory of Molecular Engineering of Polymers, Fudan University, Shanghai 200438, PR China; Yiwu Research Institute of Fudan University, Yiwu, Zhejiang 322000, PR China; International Institute for Intelligent Nanorobots and Nanosystems, Fudan University, Shanghai 200438, PR China*

Jinlong Wang − *Department of Materials Science & State Key Laboratory of Molecular Engineering of Polymers, Fudan University, Shanghai 200438, PR China; Yiwu Research Institute of Fudan University, Yiwu, Zhejiang 322000, PR China; International Institute for Intelligent Nanorobots and Nanosystems, Fudan University, Shanghai 200438, PR China*; orcid.org/0000-0002-1444-0838

Ruoyan Xu − *Department of Materials Science & State Key Laboratory of Molecular Engineering of Polymers, Fudan University, Shanghai 200438, PR China; Yiwu Research Institute of Fudan University, Yiwu, Zhejiang 322000, PR China; International Institute for Intelligent Nanorobots and Nanosystems, Fudan University, Shanghai 200438, PR China*

Yongfeng Mei − *Department of Materials Science & State Key Laboratory of Molecular Engineering of Polymers, Fudan University, Shanghai 200438, PR China; Yiwu Research Institute of Fudan University, Yiwu, Zhejiang 322000, PR China; International Institute for Intelligent Nanorobots and Nanosystems, Fudan University, Shanghai 200438, PR China*; orcid.org/0000-0002-3314-6108

Complete contact information is available at: https://pubs.acs.org/10.1021/acsami.4c01573

Author Contributions

#Z.L. and X.K. contributed equally to this work.

Notes

The authors declare no competing financial interest.

■ ACKNOWLEDGMENTS

This work was supported by the National Key Technologies R&D Program of China (Nos. 2021YFA0715302 and 2021YFE0191800), the National Natural Science Foundation of China (Nos. 61975035 and 52203328), and the Science and Technology Commission of Shanghai Municipality (22ZR1405000).

■ REFERENCES

(1) Wang, Z.; Hao, Z.; Wang, X.; Huang, C.; Lin, Q.; Zhao, X.; Pan, Y. A Flexible and Regenerative Aptameric Graphene−Nafion Biosensor for Cytokine Storm Biomarker Monitoring in Undiluted

Biofluids toward Wearable Applications. *Adv. Funct. Mater.* **2021**, *31* (4), 2005958.
(2) Yang, X.; Yi, J.; Wang, T.; Wang, T.; Feng, Y.; Wang, J.; Yu, J.; Zhang, F.; Jiang, Z.; Lv, Z.; et al.et al. Wet-Adhesive On-Skin Sensors Based on Metal−Organic Frameworks for Wireless Monitoring of Metabolites in Sweat. *Adv. Mater.* **2022**, *34*, 2201768.
(3) Ling, Y.; An, T.; Yap, L.; Zhu, B.; Gong, S.; Cheng, W. Disruptive, Soft, Wearable Sensors. *Adv. Mater.* **2020**, *32* (18), 1904664.
(4) Gao, F.; Liu, C.; Zhang, L.; Liu, T.; Wang, Z.; Song, Z.; Cai, H.; Zhen, F.; Chen, J.; Wang, J.; et al.et al. Wearable and Flexible Electrochemical Sensors for Sweat Analysis: A Review. *Microsyst. Nanoeng.* **2023**, *9*, 1.
(5) Zhang, Q.; Jiang, D.; Xu, C.; Ge, Y.; Liu, X.; Wei, Q.; Huang, L.; Ren, X.; Wang, C.; Wang, Y. Wearable Electrochemical Biosensor Based on Molecularly Imprinted Ag Nanowires for Noninvasive Monitoring Lactate in Human Sweat. *Sens. Actuators, B* **2020**, *320*, 128325.
(6) Rauf, S.; Vijjapu, M.; Andrés, M.; Gascón, I.; Roubeau, O.; Eddaoudi, M.; Salama, K. Highly Selective Metal-Organic Framework Textile Humidity Sensor. *ACS Appl. Mater. Interfaces* **2020**, *12* (26), 29999−30006.
(7) Yang, X.; Ynag, Z.; Shao, R.; Guan, R.; Dong, S.; Xie, M. Chiral MOF Derived Wearable Logic Sensor for Intuitive Discrimination of Physiologically Active Enantiomer. *Adv. Mater.* **2023**, *35*, 2304046.
(8) Kim, J.; Campbell, A.; Avila, B.; Wang, J. Wearable Biosensors for Healthcare Monitoring. *Nat. Biotechnol.* **2019**, *37*, 389−406.
(9) Feng, T.; Zhao, X.; Gu, P.; Yang, W.; Wang, C.; Guo, Q.; Long, Q.; Liu, Q.; Cheng, Y.; Li, J.; et al.et al. Adipocyte-Derived Lactate is a Signalling Metabolite that Potentiates Adipose Macrophage Inflammation via Targeting PHD_2. *Nat. Commun.* **2022**, *13*, 5208.
(10) Saha, T.; Songkakul, T.; Knisely, C.; Yokus, M.; Daniele, M.; Dickey, M.; Bozkurt, A.; Velev, O. Wireless Wearable Electrochemical Sensing Platform with Zero-Power Osmotic Sweat Extraction for Continuous Lactate Monitoring. *ACS Sens.* **2022**, *7*, 2037−2048.
(11) Torres-Torrelo, H.; Ortega-Sáenz, P.; Gao, L.; López-Barneo, J. Lactate Sensing Mechanisms in Arterial Chemoreceptor Cells. *Nat. Commun.* **2021**, *12*, 4166.
(12) Jiang, D.; Xu, C.; Zhang, Q.; Ye, Y.; Cai, Y.; Li, K.; Li, Y.; Huang, X.; Wang, Y. In-Situ Preparation of Lactate-Sensing Membrane for the Noninvasive and Wearable Analysis of Sweat. *Biosens. Bioelectron.* **2022**, *210*, 114303.
(13) Shen, L.; Liang, Z.; Chen, Z.; Wu, C.; Hu, X.; Zhang, J.; Jiang, Q.; Wang, Y. Reusable Electrochemical Non-Enzymatic Glucose Sensors Based on Au-Inlaid Nanocages. *Nano Res.* **2022**, *15*, 6490−6499.
(14) Yan, T.; Zhang, G.; Yu, K.; Chai, H.; Tian, M.; Qu, L.; Dong, H.; Zhang, X. Smartphone Light-Driven Zinc Porphyrinic MOF Nanosheets-Based Enzyme-Free Wearable Photoelectrochemical Eensor for Continuous Sweat Vitamin C Detection. *Chem. Eng. J.* **2023**, *455*, 140779.
(15) Wang, Z.; Huang, Y.; Xu, K.; Zhong, Y.; He, C.; Jiang, L.; Sun, J.; Rao, Z.; Zhu, J.; Huang, J.; et al.etal. Natural Oxidase-Mimicking Copper-Organic Frameworks for Targeted Identification of Ascorbate in Sensitive Sweat Sensing. *Nat. Commun.* **2023**, *14* (1), 69.
(16) Yang, X.; Yi, J.; Wang, T.; Feng, Y.; Wang, Y. J.; Zhang, F.; Jiang, Z.; Lv, Z.; Li, H.; Huang, T.; et al.et al. Wet-Adhesive On-Skin Sensors Based on Metal-Organic Frameworks for Wireless Monitoring of Metabolites in Sweat. *Adv. Mater.* **2022**, *34*, 2201768.
(17) Jiang, Y.; Xia, T.; Shen, L.; Ma, J.; Ma, H.; Sun, T.; Lv, F.; Zhu, N. Facet-Dependent Cu_2O Electrocatalysis for Wearable Enzyme-Free Smart Sensing. *ACS Catal.* **2021**, *11*, 2949−2955.
(18) Li, Y.; Wang, R.; Wang, G.; Feng, S.; Shi, W.; Cheng, Y.; Shi, L.; Fu, K.; Sun, J. Mutually Noninterfering Flexible Pressure-Temperature Dual-Modal Sensors Based on Conductive Metal-Organic Framework for Electronic Skin. *ACS Nano* **2022**, *16*, 473−484.
(19) Zhao, Z.; Kong, Y.; Lin, X.; Liu, C.; Liu, J.; He, Y.; Yang, L.; Huang, G.; Mei, Y. Oxide Nanomembrane Induced Assembly of a Functional Smart Fiber Composite with Nanoporosity for an Ultra-Sensitive Flexible Glucose Sensor. *J. Mater. Chem. A* **2020**, *8*, 26119−26129.
(20) Zhao, Z.; Kong, Y.; Liu, C.; Huang, G.; Xiao, Z.; Zhu, H.; Bao, Z.; Mei, Y. Atomic Layer Deposition-Assisted Fabrication of 3D Co-Doped Carbon Framework for Sensitive Enzyme-Free Lactic Acid Sensor. *Chem. Eng. J.* **2021**, *417*, 129285.
(21) Yang, J.; Yang, Y. Metal−Organic Frameworks for Biomedical Applications. *Small* **2020**, *16* (10), 1906846.
(22) Mohan, B.; Kumar, S.; Xi, H.; Ma, S.; Tao, Z.; Xing, T.; Yao, H.; Zhang, Y.; Ren, P. Fabricated Metal-Organic Frameworks (MOFs) as Luminescent and Electrochemical Biosensors for Cancer Biomarkers Detection. *Biosens. Bioelectron.* **2022**, *197*, 113738.
(23) Zhang, J.; Li, Y.; Chai, F.; Li, Q.; Wang, D.; Liu, L.; Tang, B.; Jiang, X. Ultrasensitive Point-of-Care Biochemical Sensor Based on Metal-AIEgen Frameworks. *Sci. Adv.* **2022**, *8* (30), No. eabo1874.
(24) Gu, C.; Bai, L.; Pu, L.; Gai, P.; Li, F. Highly Sensitive and Stable Self-Powered Biosensing for Exosomes Based on Dual Metal-Organic Frameworks Nanocarriers. *Biosens. Bioelectron.* **2021**, *176*, 112907.
(25) Konnerth, H.; Matsager, B.; Chen, S.; Prechtl, M.; Shieh, F.; Wu, K. Metal-Organic Framework (MOF)-Derived Catalysts for Fine Chemical Production. *Coord. Chem. Rev.* **2020**, *416*, 213319.
(26) Wang, H.; Li, X.; Lan, X.; Wang, T. Supported Ultrafine NiCo Bimetallic Alloy Nanoparticles Derived from Bimetal-Organic Frameworks: A Highly Active Catalyst for Furfuryl Alcohol Hydrogenation. *ACS Catal.* **2018**, *8*, 2121−2128.
(27) Zhao, S.; Tan, C.; He, C.; An, P.; Xie, F.; Jiang, S.; Zhu, Y.; Wu, K.; Zhang, B.; Li, H.; et al.et al. Structural transformation of highly active metal−organic framework electrocatalysts during the oxygen evolution reaction. *Nat. Energy* **2020**, *5* (11), 881−890.
(28) Ma, Y.; Leng, Y.; Huo, D.; Zhao, D.; Zheng, J.; Zhao, P.; Yang, H.; Li, F.; Hou, C. A Portable Sensor for Glucose Detection in *Huangshui* Based on Blossom-Shaped Bimetallic Organic Framework Loaded with Silver Nanoparticles Combined with Machine Learning. *Food Chem.* **2023**, *429*, 136850.
(29) Guo, Y.; Wang, K.; Hong, Y.; Wu, H.; Zhang, Q. Recent Progress on Pristine Two-Dimensional Metal-Organic Frameworks as Active Components in Supercapacitors. *Dalton Trans.* **2021**, *50*, 11331−11346.
(30) Liu, C.; Bai, Y.; Li, W.; Yang, F.; Zhang, G.; Pang, H. In Situ Growth of Three-Dimensional MXene/Metal-Organic Framework Composites for High-Performance Supercapacitors. *Angew. Chem., Int. Ed.* **2022**, *61*, No. e202116282.
(31) Mu, Z.; Wu, S.; Guo, J.; Zhao, M.; Wang, Y. Dual Mechanism Enhanced Peroxidase-like Activity of Iron-Nickel Bimetal-Organic Framework Nanozyme and Its Application for Biosensing. *ACS Sustainable Chem. Eng.* **2022**, *10*, 2984−2993.
(32) Jiang, Q.; Xiao, Y.; Hong, A.; Gao, Z.; Shen, Y.; Fan, Q.; Feng, P.; Zhong, W. Bimetallic Metal-Organic Framework Fe/Co-MIL-88(NH_2) Exhibiting High Peroxidase-like Activity and Its Application in Detection of Extracellular Vesicles. *ACS Appl. Mater. Interfaces* **2022**, *14*, 41800−41808.
(33) Ke, X.; Zhao, Z.; Huang, J.; Liu, C.; Huang, G.; Tan, J.; Zhu, H.; Xiao, Z.; Liu, X.; Mei, Y.; et al.et al. Growth Control of Metal−Organic Framework Films on Marine Biological Carbon and Their Potential-Dependent Dopamine Sensing. *ACS Appl. Mater. Interfaces* **2023**, *15*, 12005−12016.
(34) Zhao, Z.; Kong, Y.; Huang, G.; Liu, C.; You, C.; Xiao, Z.; Zhu, H.; Tan, J.; Xu, B.; Cui, J.; et al.et al. Area-Selective and Precise Assembly of Metal Organic Framework Particles by Atomic Layer Deposition Induction and Its Application for Ultra-Sensitive Dopamine Sensor. *Nano Today* **2022**, *42*, 101347.
(35) Chen, T.; Wang, F.; Cao, S.; Bai, Y.; Zheng, S.; Li, W.; Zhang, S.; Hu, S.; Pang, H. In Situ Synthesis of MOF-74 Family for High Areal Energy Density of Aqueous Nickel−Zinc Batteries. *Adv. Mater.* **2022**, *34* (30), 2201779.
(36) Barton, H.; Davis, A.; Parsons, G. The Effect of Surface Hydroxylation on MOF Formation on ALD Metal Oxides: MOF-525

https://doi.org/10.1021/acsami.4c01573
ACS Appl. Mater. Interfaces 2024, 16, 14218−14228

on TiO_2/Polypropylene for Catalytic Hydrolysis of Chemical Warfare Agent Simulants. *ACS Appl. Mater. Interfaces* **2020**, *12*, 14690−14701.
(37) Gikonyo, B.; Liu, F.; De, S.; Journet, C.; Marichy, C.; Fateeva, A. Investigating the Vapour Phase Synthesis of Copper Terephthalate Metal Organic Framework Thin Films by Atomic/Molecular Layer Deposition. *Dalton Trans.* **2023**, *52*, 211−217.
(38) Johnson, R. W.; Hultqvist, A.; Bent, S. F. A Brief Review of Atomic Layer Deposition: from Fundamentals to Applications. *Mater. Today* **2014**, *17*, 236−246.
(39) Chi, Y.; Yang, W.; Xing, Y.; Li, Y.; Pang, H.; Xu, Q. Ni/Co Bimetallic Organic Framework Nanosheet Assemblies for High-Performance Electrochemical Energy Storage. *Nanoscale* **2020**, *19*, 10685.
(40) Farha, O. K.; Eryazici, I.; Jeong, N. C.; Hauser, B. G.; Wilmer, C. E.; Sarjeant, A. A.; Snurr, R. Q.; Nguyen, S. T.; Yazaydın, A. Ö.; Hupp, J. T. Metal-Organic Framework Materials with Ultrahigh Surface Areas: Is the Sky the Limit? *J. Am. Chem. Soc.* **2012**, *134*, 15016−15021.
(41) Zeng, S.; Shi, H.; Dai, T. Y.; Liu, Y.; Wen, Z.; Han, G.; Wang, T.; Zhang, W.; Lang, X.; Zheng, W.; et al.et al. Lamella-Heterostructured Nanoporous Bimetallic Iron-Cobalt Alloy/oxy-hydroxide and Cerium Oxynitride Electrodes as Stable Catalysts for Oxygen Evolution. *Nat. Commun.* **2023**, *14* (1), 1811.
(42) Ravel, B.; Newville, M. ATHENA, ARTEMIS, HEPHAESTUS: Data Analysis for X-ray Absorption Spectroscopy Using IFEFFIT. *J. Synchrotron Radiat.* **2005**, *12*, 537−541.
(43) Qiu, Y.; Zhang, J.; Jin, J.; Sun, J.; Tang, H.; Chen, Q.; Zhang, Z.; Sun, W.; Meng, G.; Xu, Q.; et al.et al. Construction of Pd-Zn Dual Sites to Enhance the Performance for Ethanol Electro-Oxidation Reaction. *Nat. Commun.* **2021**, *12* (1), 5273.
(44) Funke, H.; Scheinost, A.; Chukalina, M. Wavelet Analysis of Extended X-ray Absorption Fine Structure Data. *Phys. Rev. B* **2005**, *71*, 094110.
(45) Funke, H.; Chukalina, M.; Scheinost, A. A New FEFF-Based Wavelet for EXAFS Data Analysis. *J. Synchrotron Radiat.* **2007**, *14*, 426−432.
(46) Kresse, G.; Furthmüller, J. Efficient Iterative Schemes for AB Initio Total-Energy Calculations Using a Plane-Wave Basis Set. *Phys. Rev. B* **1996**, *54*, 11169−11186.
(47) Perdew, J.; Ernzerhof, M.; Burke, K. Rationale for Mixing Exact Exchange with Density Functional Approximations. *J. Chem. Phys.* **1996**, *105*, 9982−9985.

https://doi.org/10.1021/acsami.4c01573
ACS Appl. Mater. Interfaces 2024, 16, 14218−14228